

# Higher-order mode grating devices in $\text{As}_2\text{S}_3$ chalcogenide glass rib waveguides

Klaus Finsterbusch, Neil J. Baker, Vahid G. Ta'eed, and Benjamin J. Eggleton

*Centre for Ultrahigh-bandwidth Devices for Optical Systems (CUDOS), School of Physics, University of Sydney, Sydney, New South Wales 2006, Australia*

Duk-Yong Choi, Steve Madden, and Barry Luther-Davies

*Centre for Ultrahigh-bandwidth Devices for Optical Systems (CUDOS), Laser Physics Centre, Australian National University, Canberra, Australian Capital Territory 0200, Australia*

Received November 8, 2006; revised January 31, 2007; accepted February 13, 2007;  
posted March 1, 2007 (Doc. ID 76886); published May 17, 2007

We report on the design and fabrication of high-quality long-period gratings in chalcogenide glass ( $\text{As}_2\text{S}_3$ ) rib waveguides utilizing the strong photosensitivity. Higher-order modes of the rib waveguides are analyzed by inspection of the spectra of Bragg gratings written into these waveguides. Based on these measurements, we infer the effective indices of higher-order modes, which are in good agreement with modeling results using a beam propagation method. High-quality long-period gratings are then designed and written into the rib waveguides using a simple shadow mask technique. Coupling the fundamental to the  $\text{HE}_{02}$  mode strong resonances of up to  $\sim 20$  dB depths are obtained. The gratings have a length of  $L=26$  mm and a period of  $\Lambda=86$   $\mu\text{m}$ . *In situ* monitoring of the writing process allows the growth dynamics of the grating to be studied. A theoretical fit to the measured transmission curve gives an average index change of  $\sim 10^{-3}$ . © 2007 Optical Society of America

OCIS codes: 350.2770, 160.3130, 130.3120.

## 1. INTRODUCTION

Long- and short-period (Bragg)-grating devices are of great importance for optical communication systems, where they act as filters, multiplexers, dispersion compensators, and gain equalizers, as well as for sensing applications (see 1 and references therein). Long-period gratings (LPGs) are attractive because of their low insertion loss, i.e., low backreflection, and ease of fabrication. In addition, they offer important solutions for applications requiring tunability and sensing. The latter properties are associated with the copropagating geometry, which manifests in an increased sensitivity, compared with Bragg-grating devices. In an optical-fiber-based LPG the grating induces coupling from the fundamental mode, localized to the core region, to the higher-order cladding modes, confined by the outer air cladding. Such LPGs typically have periods of hundreds of micrometers and can be written in photosensitive fiber using simple modifications to the interferometric techniques used for writing Bragg gratings.<sup>2</sup> Optical-fiber-based LPGs have been convincingly demonstrated for a range of applications, including optical filters,<sup>3,4</sup> mode converters,<sup>5</sup> optical gain flattening of erbium-doped fiber amplifiers,<sup>6</sup> dispersion compensation,<sup>7</sup> and sensing.<sup>8</sup> LPGs are of particular interest for all-optical switching devices<sup>9</sup> where the intensity-dependent refractive index associated with the Kerr effect ( $n_2$ ) can be used to detune the resonance wavelength resulting in intensity-dependent transmission.<sup>10</sup>

Chalcogenide glasses have generated significant interest due to their many attractive features. Their high

transparency in the near-infrared and mid-infrared and exceptionally high Kerr nonlinearity ( $n_2$  up to 3 orders of magnitude greater than silica<sup>11</sup>) combined with an intrinsic response time of less than 100 fs and moderate two-photon absorption makes chalcogenide glasses suitable for a variety of applications ranging from infrared delivery,<sup>12</sup> Raman fiber lasers and amplifiers in the mid-infrared,<sup>11,13</sup> to all-optical signal regeneration<sup>14</sup> and switching.<sup>15</sup> Chalcogenides possess strong photosensitivity that allows for the inscription of ultrastrong Bragg gratings in chalcogenide fiber<sup>16</sup> and rib waveguides.<sup>17,18</sup> LPGs in chalcogenide glass waveguides are promising candidates for low threshold all-optical switching devices and have recently been demonstrated in single-mode  $\text{As}_2\text{S}_3$  fibers based on microbends<sup>19</sup> and acoustic modulation of the core index.<sup>20</sup>

Long-period gratings in planar-integrated geometries<sup>21</sup> offer greater flexibility than fiber LPGs as they can be fabricated in a wide variety of optical materials including glasses,<sup>22</sup> polymers,<sup>23</sup> and semiconductors. These materials and geometries offer novel transmission characteristics,<sup>24</sup> enhanced thermal tunability,<sup>22</sup> and the potential for integrated reconfigurable electro-optical-induced gratings.<sup>25</sup> More recently, LPGs have been demonstrated in chalcogenide ( $\text{As}_2\text{S}_3$ ) glass rib waveguides.<sup>26</sup> This geometry is a promising candidate for compact, integrated resonant devices for a range of applications, including low-threshold, all-optical switching devices, integrated Raman devices, and mid-infrared applications.

Following our recent report,<sup>26</sup> here we present a de-

tailed investigation of the design, fabrication, and characterization of high-quality LPGs in highly nonlinear chalcogenide glass ( $\text{As}_2\text{S}_3$ ) rib waveguides. The mode structure of the waveguides is analyzed by careful inspection of the spectra of Bragg gratings<sup>27</sup> written into these waveguides with a scanning Sagnac interferometer.<sup>18</sup> The effective indices of the higher-order modes are inferred from the Bragg-grating spectra and compared with results of numerical simulations obtained using a beam propagation method.<sup>28</sup> Applying this powerful approach to chalcogenide glass rib waveguides for the first time, we are able to accurately design LPGs with resonances at telecommunication wavelengths. Additionally the growth dynamic is studied for its implications on future switching experiments in this geometry. LPGs are fabricated exploiting a simple shadow mask technique utilizing the photosensitivity of  $\text{As}_2\text{S}_3$  chalcogenide glass to green light (532 nm). We achieve up to 20 dB deep, 5 nm (−3 dB) wide band rejection at 1564 nm finding good agreement with theory. These results are promising for future low power, nonlinear switching devices and as building blocks for mid-infrared technologies, including Raman devices.

The paper is structured as follows. Section 2 gives a brief review of the theoretical background of short- and long-period gratings as well as the Bragg-grating-based procedure of mode analyses. Section 3 deals with the waveguide fabrication and mode properties. In Section 4, experimental results on long-period grating fabrication and growth dynamics are presented.

## 2. REVIEW OF MODE COUPLING IN WAVEGUIDE GRATINGS

In this paper, we focus on higher-order mode (HOM) coupling in multimode rib waveguides via grating-induced phase matching. Figure 1(a) depicts the structure of a rib waveguide, consisting of substrate, film layer, and cladding with refractive indices  $n_s$ ,  $n_f$ , and  $n_c$ , respectively, together with the profiles of the fundamental and first horizontal and vertical higher-order modes with respective propagation constant  $\beta$ . Figures 1(b) and 1(c) illustrate how a grating with period  $\Lambda$  allows energy to be coupled between two contrapropagating or copropagating modes, provided that the following phase-matching condition is met:

$$\Delta\beta = \beta_i \pm \beta_f - \frac{2\pi}{\Lambda} \equiv 0. \quad (1)$$

Here “+” and “−” are valid for coupling between contrapropagating and copropagating modes, and  $\Delta\beta$  denotes a phase mismatch.<sup>29</sup> As can be seen from Figs. 1(b) and 1(c), the coupling of contrapropagating modes requires a large grating vector and hence a short-period grating (Bragg grating), whereas a long-period grating couples two copropagating modes so that the grating vector is small.

From the phase-matching condition [Eq. (1)] it follows that the resonance wavelength for coupling the  $m$ th forward-propagating mode to the  $n$ th backward-propagating mode is given by

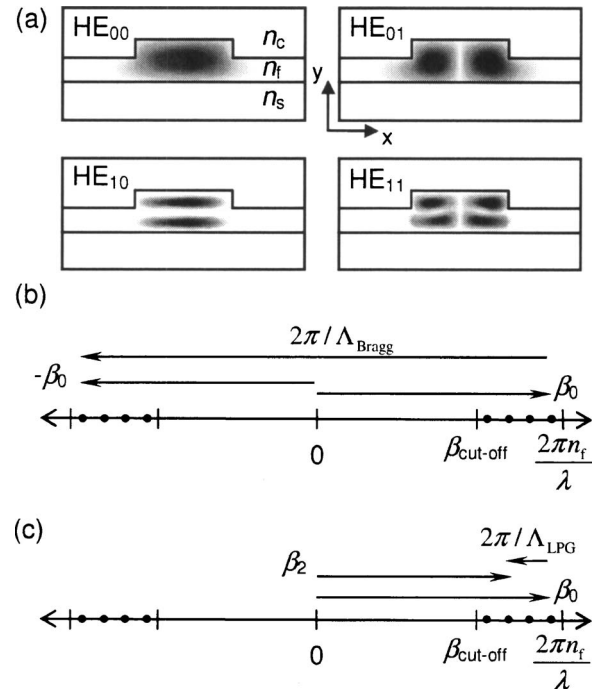


Fig. 1. (a) Schematic of a rib waveguide and the transverse profile of the first HOMs, (b) and (c) relative position of the propagation constants in a rib waveguide (after [29]). Solid symbols: guided modes.

$$\lambda_{m,n} = \Lambda(N_m + N_n), \quad (2)$$

where  $N_m$  and  $N_n$  are the effective indices of the two modes involved. If degenerate coupling between the fundamental modes this reduces to the well-known Bragg condition

$$\lambda_0 = 2\Lambda N_0. \quad (3)$$

Higher-order mode resonances due to coupling the fundamental mode to the  $n$ th HOM can be used to investigate the mode properties of the HOMs. Combining Eqs. (2) and (3), the ratio of the HOM to fundamental resonance wavelengths is given as

$$\frac{\lambda_{0,n}}{\lambda_0} = \frac{N_0 + N_n}{2N_0}. \quad (4)$$

Neglecting material and waveguide dispersion Eq. (4) can be used to infer the effective indices of the first few HOMs, by simple inspection of the Bragg-grating spectrum, provided the grating period  $\Lambda$  is known to infer  $N_0$  via Eq. (3).

Similar to Eq. (2), the resonance wavelength of a LPG that couples light between the fundamental mode and the  $m$ th HOM is given by

$$\lambda_0 = \Lambda(N_0 - N_m). \quad (5)$$

Provided that the HOM exhibits low linear transmission, this coupling can manifest a dip in the transmission spectrum centered at the wavelengths given by Eq. (5).

It follows from coupled-mode theory<sup>30</sup> that the variation of the power in the fundamental mode with the propagation distance  $z$  is given as

$$P(z) = P_0 \left( 1 - \frac{\kappa^2}{\gamma^2} \sin^2 \gamma z \right), \quad (6)$$

where  $\gamma^2 = \kappa^2 + (\Delta\beta/2)^2$ , and  $\kappa$  denotes the coupling coefficient that is dependent on the symmetry of the interacting modes and LPG. It can be seen from Eq. (6) that the power in the fundamental mode shows an oscillatory behavior with a period  $\pi\kappa^{-1}$  (for  $\Delta\beta=0$ ). Maximum coupling occurs when  $\kappa z$  equals an odd multiple of  $\pi/2$ , while  $\kappa z > \pi/2$  leads to overcoupling, resulting in strong sidelobes.<sup>29</sup>

The coupling coefficient  $\kappa$  is given as<sup>27</sup>

$$\kappa = \frac{n}{\lambda} \iint F_n(x,y) \Delta n(x,y) F_m^*(x,y) dx dy, \quad (7)$$

where the modal field distribution is given by  $F(x,y)$ . For uniform LPGs, the resonance can be fitted by Eq. (6) to give a value for  $\kappa$ . Thus the index change can be derived from Eq. (7) using mode fields obtained from numerical simulation.

### 3. WAVEGUIDE STRUCTURE AND MODE ANALYSIS

#### A. Waveguide Fabrication and Properties

Figure 2(a) is a schematic of the transverse profile of the chalcogenide glass ( $\text{As}_2\text{S}_3$ ) rib waveguide while Fig. 2(b) is a scanning electron micrograph (SEM) of a typical sample. The waveguides were fabricated by ultrafast pulsed laser deposition<sup>31</sup> of an  $\sim 3 \mu\text{m}$  thick  $\text{As}_2\text{S}_3$  film on a silicon wafer with a  $2.5 \mu\text{m}$  thick thermal oxide layer, followed by photolithography and reactive-ion etching<sup>32</sup> to form 5 cm long rib waveguides. The wafer is then coated with a protective polysiloxane film (thickness  $>10 \mu\text{m}$ ) transparent to visible light. The rib height  $H$ , slab height  $h$ , and width  $W$  is determined from the electron micrographs with an accuracy of approximately  $\pm 5\%$ , due to the calibration error of the SEM, giving  $H=2.56 \mu\text{m}$ ,  $h=1.53 \mu\text{m}$ , and  $W=6.45 \mu\text{m}$  averaged over five waveguides. The propagation loss has been reported to be as low as  $0.25 \text{ dB/cm}$  at  $1.55 \mu\text{m}$ .<sup>32</sup> The refractive indices

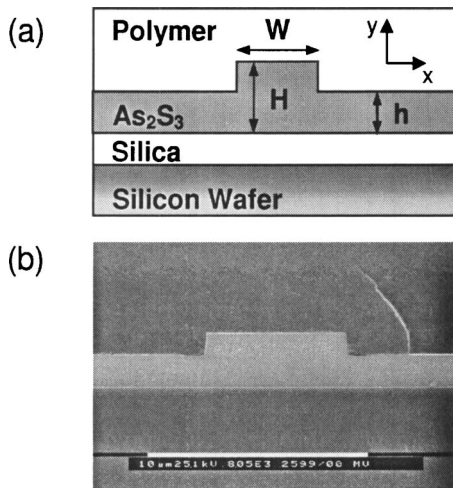


Fig. 2. (a) Schematic of the  $\text{As}_2\text{S}_3$  rib waveguide sample and (b) a scanning-electron microscope image of a waveguide.

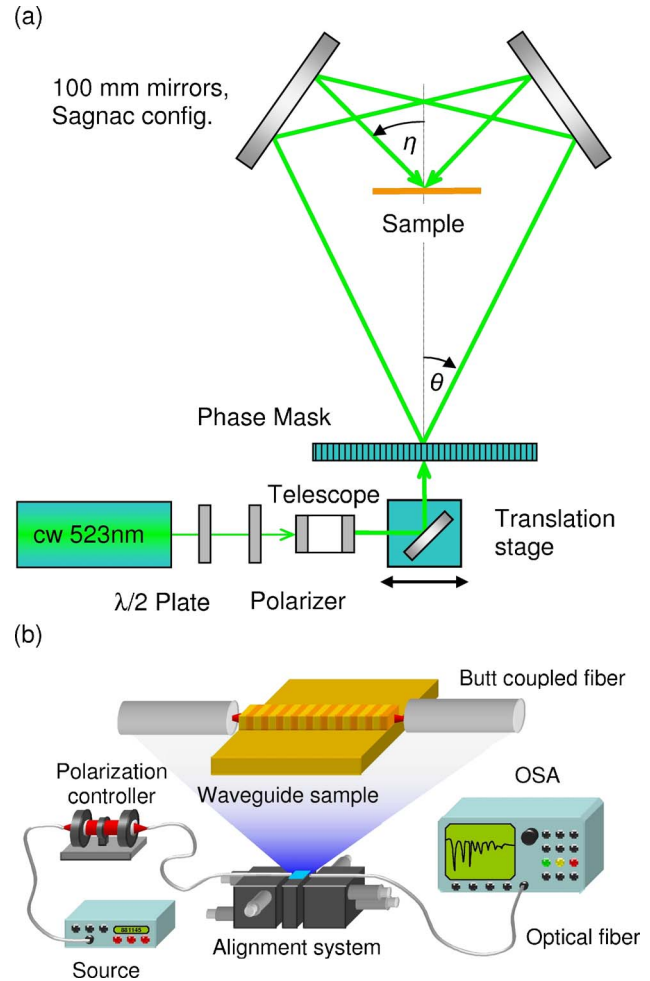


Fig. 3. (Color online) (a) Schematic of the Bragg-grating writing setup based on the modified Sagnac interferometer and (b) analyzing setup.

$n_s$ ,  $n_f$ , and  $n_c$  of the substrate ( $\text{SiO}_2$ ), film ( $\text{As}_2\text{S}_3$ ), and cladding (polymer) are 1.44, 2.38, and 1.53, respectively. It follows from the single-mode condition given by Soref *et al.*<sup>33</sup> that these waveguides support several HOMs, which we exploit for resonant coupling devices.

#### B. Bragg-Grating Writing Setup

Because of the forward coupling geometry in an LPG, its resonance wavelength strongly depends on the waveguide parameters, which are measured with an accuracy of  $\pm 5\%$ . This uncertainty can lead to unacceptable deviations of the LPG resonance from the design wavelength. To minimize the uncertainties of the resonance wavelength, the effective indices of the rib modes are inferred by careful analysis of a Bragg-grating spectrum as per Section 2. For this purpose, the 50 mm waveguide sample was cleaved into two, and Bragg gratings were written into the shorter 20 mm section. LPGs were written into the longer 30 mm section as described in the following section.

The Bragg-grating writing setup shown in Fig. 3(a) is based on a modified Sagnac interferometer design as previously described by Shokooh-Saremi *et al.*<sup>17</sup> The beam of a cw frequency-doubled Nd:YAG laser at a wavelength of  $532 \text{ nm}$  is spatially filtered and collimated before passing

through a phase mask. The equal intensity  $\pm 1$  orders of the phase mask are reflected by a pair of mirrors and interfere on the surface of the vertical mounted sample. As the photon energy of the writing laser is close to the bandgap energy of  $\text{As}_2\text{S}_3$  chalcogenide glass (corresponding to a wavelength of  $\sim 514$  nm), the resulting fringe pattern produces a photoinduced periodic change in the refractive index. Scanning the incident beam across the phase mask causes the point of intersection to move along the waveguide whereas the fringe pattern is fixed.<sup>18</sup> The current setup allows for a grating length of 37 mm only limited by the 25 mm travel of the translation stage. The maximum power in each interferometer arm is  $\sim 5$  mW each in an  $\sim 1.5$  mm spot on the sample. The grating strength is controlled by the scanning speed and/or the power of the writing laser that can be varied by a combination of  $\lambda/2$  plate and linear polarizer. The period  $\Lambda$  of the written grating is  $\Lambda = \lambda_w/2 \sin(\eta)$ ,<sup>17</sup> where  $\eta$  is the half-angle between the two interfering beams, and  $\lambda_w$  is the wavelength of the writing laser.  $\eta$  has been measured geometrically to be  $53.81^\circ$  resulting in a grating period of  $\Lambda = 329.6$  nm. The setup allows for *in situ* monitoring during the writing process as shown in Fig. 3(b). The broadband amplified spontaneous emission (ASE) of an erbium-doped fiber amplifier passes a polarizer and  $\lambda/4$  plate and is transmitted through the waveguide by standard single-mode fiber pigtailed but coupled to the waveguide. The coupling efficiency is enhanced by a short piece of ultrahigh NA fiber spliced to the fiber pigtailed. The transmitted light is then analyzed with a 10 pm resolution optical spectrum analyzer.

### C. Mode Analysis

Figure 4 shows the transmission spectrum for both TE- and TM-polarized light of a Bragg grating written into a 20 mm long waveguide. The grating has a length of 15 mm and is written with a scanning speed of 0.015 mm/s on the sample and a total power of  $\sim 2$  mW. The fundamental resonance for TE polarization at  $\lambda_0$

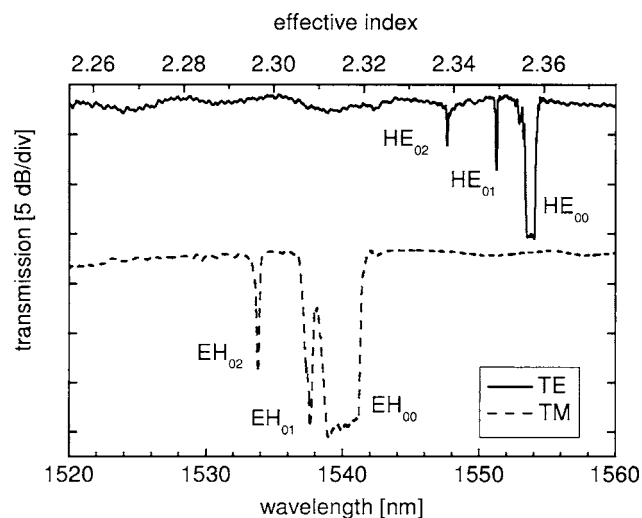


Fig. 4. Normalized transmission spectrum of a 15 mm long Bragg grating for TE- and TM-polarized light written into a  $6.45 \mu\text{m}$  wide and 20 mm long waveguide ( $H = 2.56 \mu\text{m}$ ,  $h = 1.53 \mu\text{m}$ ). The upper axis shows the refractive indices as they were inferred from the spectrum.

**Table 1. Comparison Between the Effective Indices Inferred From the Bragg Grating in Fig. 4 and Those Obtained With the Beam Propagation Method**

Polarization	Mode	Experiment		Simulation	
		$\lambda_{\text{exp}}$ (nm)	$N_{\text{exp}}$	$\lambda_{\text{BPM}}$ (nm)	$N_{\text{BPM}}$
TE $n = 2.3757$	$\text{HE}_{00}$	1553.8	2.3571	1553.7	2.3570
	$\text{HE}_{01}$	1551.2	2.3494	1551.3	2.3496
	$\text{HE}_{02}$	1547.6	2.3384	1547.6	2.3384
TM $n = 2.3757$	$\text{EH}_{00}$	1539.8	2.3359	1552.4	2.3550
	$\text{EH}_{01}$	1537.6	2.3293	1550.0	2.3476
	$\text{EH}_{02}$	1533.8	2.3178	1546.1	2.3359
TM $n = 2.3566$	$\text{EH}_{00}$	1539.8	2.3359	1539.8	2.3358
	$\text{EH}_{01}$	1537.6	2.3293	1537.3	2.3284
	$\text{EH}_{02}$	1533.8	2.3178	1533.4	2.3166

= 1553.77 nm has a width of  $\Delta\lambda = 0.7$  nm corresponding to an index change of  $\Delta n = 10^{-3}$ . There are two additional resonances visible on the short wavelength side of the fundamental resonance due to coupling the fundamental waveguide mode to backward-propagating HOMs. As material and waveguide dispersion can be neglected over the shown spectral range, the effective indices of the HOMs can simply be inferred from the resonance wavelengths as described in Subsection 2 providing a powerful tool for designing the LPG.

From Eq. (3) and the measured wavelength of the fundamental resonance, the effective index of the fundamental mode is determined to be  $N_0 = 2.3571$  for TE polarization. Table 1 lists the experimental results for both the TE and TM modes together with simulation results obtained with a beam propagation method.<sup>28</sup> For TE-polarized light, the theoretical results show good agreement with the experimental values. This is achieved by using a slightly smaller value for the slab height  $h$  in the simulations motivated by the grooves to either side of the waveguide rib as visible in the SEM image in Fig. 2(b). The depth of these grooves is  $\sim 0.1 \mu\text{m}$  so that the slab height experienced by a waveguide mode is reduced affecting the mode indices. The measured effective indices are best approximated with a reduced slab height of  $h = 1.45 \mu\text{m}$ .

The discrepancy between the calculated and measured effective indices in case of TM-polarized light is most likely due to birefringence in the  $\text{As}_2\text{S}_3$  thin film. The measured indices can be fitted with reasonable accuracy by use of a material refractive index for TM of  $n^{\text{TM}} = 2.3566$  compared with  $n^{\text{TE}} = 2.3757$  for TE-polarized light. As the electric field vector for TE respective TM waves is mainly polarized in the  $x$  respective  $y$  direction, with the definition of Fig. 1(a), this leads to a material birefringence of  $\Delta n = n_x - n_y \approx 0.02$ . This can be partially understood by noting that from the ultrafast laser deposition process the evaporated material forms layers on the wafer.<sup>34</sup> In such a layered structure, the electronic bondings are mainly orientated within the layer rather than perpendicular to it, leading to a smaller polarizability in the  $y$  direction. Thus the refractive index for  $y$ -polarized light is reduced.

## 4. PROPERTIES OF THE LONG-PERIOD GRATINGS

### A. Fabrication of Long-Period Gratings

The LPG writing and analyzing setup shown in Fig. 5 is a modification of the setup used for Bragg-grating fabrication. The periods of the waveguide LPGs are of the order of tens of micrometers, allowing the modified Sagnac interferometer to be replaced by a shadow mask. The shadow mask consists of a photolithographically patterned chrome layer on a quartz substrate. The mask is 26 mm  $\times$  135 mm and contains 14 patterns with periods varying from 48 to 102  $\mu\text{m}$  (50% duty cycle) in steps of 2  $\mu\text{m}$ . The mask is placed in contact to the waveguide sample with the chromium layer facing the sample to minimize diffraction. The waveguide is then exposed to green cw light (532 nm) from a frequency-doubled, diode-pumped, Nd:YAG laser. The Gaussian laser beam is expanded to a diameter of  $\sim 70$  mm and the central 26 mm diameter is then focused by a cylindrical lens producing a  $\sim 0.01$  mm  $\times$  26 mm line focus on the stationary mask and waveguide sample. The average power onto the mask can be varied by a combination of a half-wave-plate and a polarizing beam splitter. The spectral response of the LPGs is measured in the same way as for the Bragg gratings allowing for *in situ* monitoring of the writing process [Fig. 3(b)].

### B. Coupling to Higher-Order Modes

We focus on coupling the fundamental  $\text{HE}_{00}$  mode to the  $\text{HE}_{02}$  mode, because it is the first HOM with the same symmetry as the fundamental mode. In this experiment, a 30 mm long waveguide is used. As the  $\text{HE}_{02}$  mode is well guided, the transmission loss at the resonance wavelength is due to the waveguide-to-fiber coupling loss at the output of the sample. The overlap integral of the waveguide  $\text{HE}_{00}$  fundamental mode and the higher-order  $\text{HE}_{02}$  mode with the ultrahigh NA fiber are calculated to be  $-3$  and  $-18$  dB, respectively. Thus the maximum waveguide-to-fiber coupling loss expected from modeling is  $-15$  dB assuming perfect alignment of the output fiber to the waveguide.

Using the effective indices obtained from Bragg-grating analysis and modeling (Section 3), the grating period  $\Lambda_{\text{LPG}}$  for coupling between the two modes at a design wavelength of 1.55  $\mu\text{m}$  is calculated to be  $\sim 83$   $\mu\text{m}$  for TE polarization. From the available masks, a grating pitch of  $\Lambda = 84$   $\mu\text{m}$  is chosen for the experiment. The power of the writing laser incident on the mask was 1 mW. Figure 6

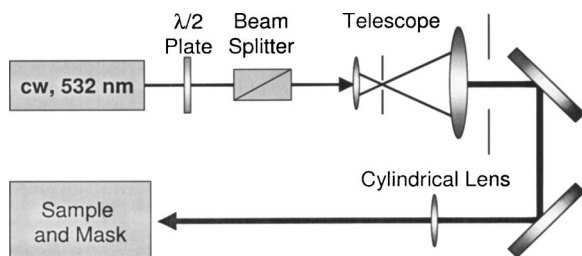


Fig. 5. Schematic of the LPG writing setup.

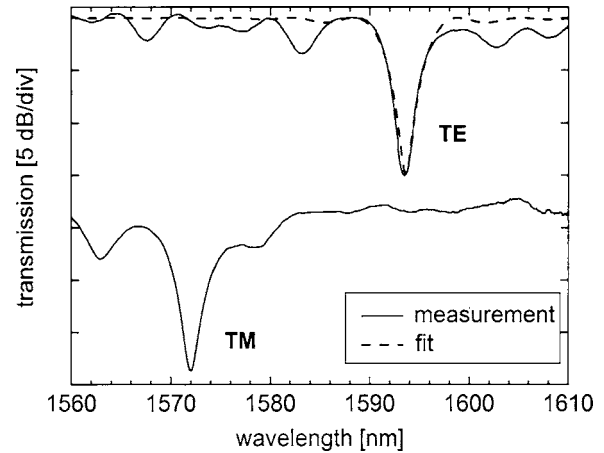


Fig. 6. Normalized transmission spectrum of a 26 mm long LPG with a period of 84  $\mu\text{m}$  for TE- and TM-polarized light written into a 6.45  $\mu\text{m}$  wide and 30 mm long waveguide ( $H = 2.56$   $\mu\text{m}$ ,  $h = 1.53$   $\mu\text{m}$ ) exposed to 1 mW writing power at 532 nm for 70 s. The dashed curve is a fit to the measured transmission using Eq. (11).

shows the transmission spectrum for both TE- and TM-polarized light obtained by normalizing the grating spectrum to that of the bare waveguide after an exposure time of 70 s. The  $-15$  dB deep, TE- and TM-polarization resonances appear at 1593 and 1572 nm with respective  $-3$  dB widths of 5 and 7 nm. The exposure was stopped here in order not to overcouple the grating. From the dispersion curves of the waveguide obtained with the beam propagation method, the resonance wavelength is calculated to be 1537 and 1485 nm, where the birefringence of the  $\text{As}_2\text{S}_3$  film discussed in Subsection 3.C, i.e., the different material refractive indices for TE- and TM-polarized light, has been taken into account. The discrepancy between measured and predicted wavelength is most likely due to slightly varying parameters of the waveguides used for mode analysis and LPG experiment that strongly affect the effective indices. According to Eq. (5), the resonance wavelength is determined by the difference  $\Delta N = N_0 - N_m$  of the effective indices of the two coupled modes and is very sensitive to slight variations of the effective indices; variations in  $\Delta N$  as small as  $10^{-4}$  can shift the resonance by 15 nm.

Similar to the Bragg grating discussed in Subsection 3.C, the LPG resonance shown in Fig. 6 shows TE–TM-polarization splitting, which is 21 nm. In case of the Bragg grating, it turned out that the observed polarization splitting is mainly caused by material birefringence (see discussion in Subsection 3.C) rather than geometrical effects. But in the case of the LPG, the contribution of the geometrical effects, i.e., waveguide birefringence, to the polarization splitting can be expected to be much larger. Unlike the Bragg grating, the resonance wavelength of a LPG is governed by the difference of the mode indices,  $\Delta N = N_0 - N_m$  and therefore has much larger sensitivity to slight differences of the mode indices due to TE and TM polarization. This can be seen from simulations with and without taking material birefringence into account. Using the material refractive indices for TE- and TM-polarized light as inferred from the Bragg grating discussed in Subsection 3.C, i.e.,  $n^{\text{TE}} = 2.3757$  and  $n^{\text{TM}} = 2.3566$ , respec-

tively, the polarization splitting is calculated to be 52 nm for the LPG, whereas it is 42 nm for  $n^{\text{TE}}=n^{\text{TM}}=2.3757$ . Thus in the simulation, the wavelength splitting due to geometrical effects, i.e., waveguide birefringence, is four times the splitting due to material birefringence.

The dashed curve in Fig. 6 is a fit to the measured data using a slight modification of Eq. (6),

$$P(z) = P_0 \left( 1 - \frac{|S_{2,\text{UHNA}}|^2 \kappa^2}{|S_{0,\text{UHNA}}|^2 \gamma^2 \sin^2 \gamma z} \right), \quad (8)$$

where  $\kappa$  is a fit parameter, and  $|S_{m,\text{UHNA}}|^2$  is the overlap integral between the  $m$ th waveguide mode and the fundamental mode of the ultrahigh NA fiber at the end of the device. The grating period has been set to  $81 \mu\text{m}$  to fit the resonance wavelength, and waveguide dispersion obtained from modeling has been taken into account. There is no sign of broadening of the resonance proving the quality of the  $\text{As}_2\text{S}_3$  rib waveguides used in the experiment, i.e., the lack of variations in the waveguide geometry along the  $z$  direction of the specific guide. From the fit, we obtain  $\kappa=58 \text{ m}^{-1}$  and hence  $\kappa L=0.96 \times \pi/2$ , showing that coupling to the HOM is almost at maximum. The index change can be inferred from Eq. (7) with the overlap integral evaluated over the central rib region where the index change is assumed to be homogenous and zero in the slab. With the modeled mode profiles and measured coupling coefficient above the index change,  $\Delta n$  is calculated to be  $\sim 10^{-3}$  in good agreement with previously published values.<sup>17</sup>

The energy transfer from the fundamental to the  $\text{HE}_{02}$  mode is verified by mode imaging. This is done by replacing the broadband ASE source in Fig. 3(b) by a tunable cw diode laser and the output stage by an imaging system using a  $40\times$  microscope objective and an infrared CCD camera. Figures 7(a) and 7(b) depict the transversal profile of the transmitted TE-polarized light at the end facet of the

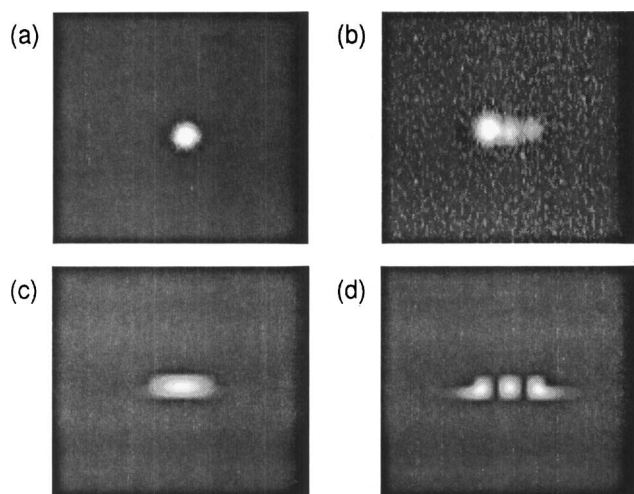


Fig. 7. Mode profiles of TE-polarized light of a tunable diode laser source at the output facet of the waveguide (a) of resonance and (b) on resonance and comparison to the calculated mode profiles (c)  $\text{HE}_{00}$  and (d)  $\text{HE}_{02}$ .

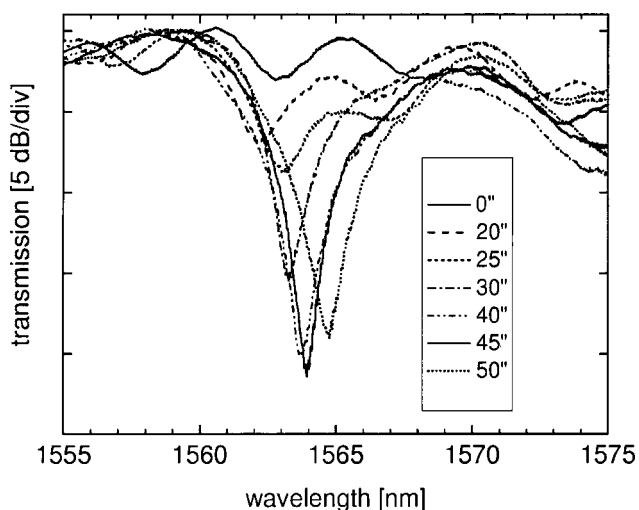


Fig. 8. Normalized transmission spectrum of a 26 mm long LPG with a period of  $86 \mu\text{m}$  for TE-polarized light at different exposure times for 1 mW writing power at 532 nm.

waveguide-tuned off and on resonance, respectively, together with the calculated profiles of mode (c)  $\text{HE}_{00}$  and (d)  $\text{HE}_{02}$ . Off resonance, the profile is that of an  $\text{HE}_{00}$  mode whereas in the center of the resonance a three-peak structure appears due to coupling most of the power to the higher-order mode.

Figure 8 shows a series of transmission spectra of an LPG with a period of  $86 \mu\text{m}$  at different exposure times for TE-polarized light. The resonance appears at 1564 nm and reaches its maximum depth of  $-20$  dB after an exposure time of 45 s. The higher loss of 20 dB, compared with 15 dB expected from modeling, is very likely due to a shift of the output fiber affecting the overlap integrals of the waveguide  $\text{HE}_{00}$  fundamental mode and the higher-order  $\text{HE}_{02}$  mode with the ultrahigh NA fiber at device output. A fit to the transmission spectrum after 45 s exposure gives  $\kappa L=\pi/2$ , i.e., optimal coupling. For stronger gratings, the power begins to couple back to the fundamental mode as indicated by the 50 s exposure.

For each transmission spectrum of the series shown in Fig. 8, the coupling coefficient is inferred and shown in Fig. 9 as a function of the exposure time. The corresponding index change  $\Delta n$  is also shown on the right scale. It can be seen that both quantities depend linearly on the exposure time, i.e., fluence, showing no sign of index saturation within the covered range. The increase of the average refractive index with exposure time causes a shift of the resonance toward larger wavelengths. This wavelength shift versus the inferred index change is plotted in the inset of Fig. 9 showing a linear dependency as expected from modeling. The rate of the wavelength shift derived from this measurement is  $\Delta\lambda/\Delta n=4.3 \times 10^3 \text{ nm}$ . This has important implications on switching experiments in these structures, where the intensity-dependent refractive index  $n=n_0+n_2I$  is used to shift the resonance wavelength of the LPG by up to one half-width of the resonance resulting in a significant increase in transmission of an initially resonant pulse. For the LPGs under investigation, the resonance wavelength has to be shifted by  $\sim 2 \text{ nm}$  to tune a pulse off resonance. With the measured rate of the wavelength shift and a Kerr coefficient

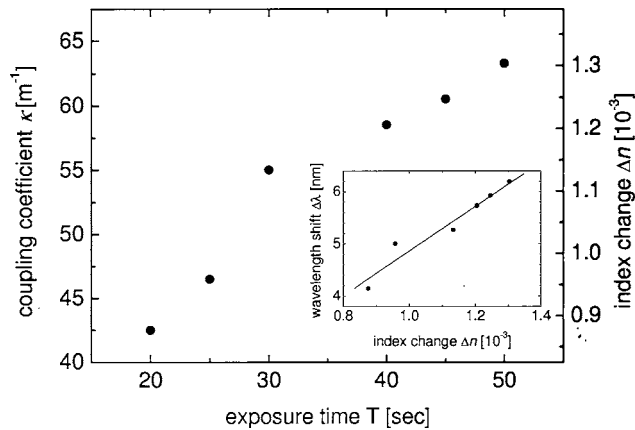


Fig. 9. Coupling coefficients and index change for the grating spectra of Fig. 8 as a function of the exposure time. Inset: induced wavelength shift versus index change.

$n_2$  in  $\text{As}_2\text{S}_3$  chalcogenide glass of  $\sim 100 \times$  silica,<sup>32</sup> the intensity-dependent wavelength shift is  $\Delta\lambda$  (nm)  $\approx I$  (GW/cm<sup>2</sup>). Thus pulse intensities of the order of 1 GW/cm<sup>2</sup> are sufficient for a significant increase in transmission.

## 5. CONCLUSION

We reported on the fabrication of high-quality long-period gratings (LPGs) in chalcogenide ( $\text{As}_2\text{S}_3$ ) glass rib waveguides at telecommunication wavelength. To design the grating, the effective indices of the higher-order modes supported by the waveguide were determined from the higher-order resonances of a holographic Bragg grating showing good agreement with modeling results using a beam propagation method. A simple shadow mask technique utilizing the photosensitivity of chalcogenide glass to green light was used to write the LPGs. A 26 mm long LPG with a grating pitch of 84  $\mu\text{m}$  written into a 30 mm long waveguide of 6.45  $\mu\text{m}$  width led to a strong resonance at 1593 and 1572 nm for TE- and TM-polarized light, respectively. The observed polarization splitting is mainly caused by the waveguide geometry. The  $-15$  dB band rejection agrees well with the maximum value expected from the mode overlap at the output of the device. The  $-3$  dB width is  $\sim 5$  nm underlining the uniformity of the waveguide and grating. A fit to the measured transmission curve yielded a coupling coefficient of  $\kappa = 58 \text{ m}^{-1}$  and index change of  $\sim 10^{-3}$ . *In situ* monitoring allowed for investigation of the grating growth dynamic. The observed wavelength shift shows a linear dependency on the index change as expected from modeling. The inferred rate of index change has significant implications for future switching experiments in these structures.

## ACKNOWLEDGMENTS

This work was produced with the assistance of the Australian Research Council (ARC). The Centre for Ultrahigh-bandwidth Devices for Optical Systems (CUDOS) is an ARC Centre of Excellence. K. Finsterbusch is a research fellow of the German Research Foundation (DFG).

The corresponding author, B. J. Eggleton, can be reached via e-mail at [egg@physics.usyd.edu.au](mailto:egg@physics.usyd.edu.au).

## REFERENCES

1. A. Othonos and K. Kalli, *Fiber Bragg Grating* (Artech House, 1999).
2. G. Meltz, W. W. Morey, and W. H. Glenn, "Formation of Bragg gratings in optical fibers by a transverse holographic method," *Opt. Lett.* **14**, 823–825 (1989).
3. A. M. Vengsarkar, P. J. Lemaire, J. B. Judkins, V. Bhatia, T. Erdogan, and J. E. Sipe, "Long-period fiber gratings as band-rejection filters," *J. Lightwave Technol.* **14**, 58–65 (1996).
4. A. Abramov, B. J. Eggleton, J. A. Rogers, R. P. Espindola, A. Hale, R. S. Windeler, and T. A. Strasser, "Electrically tunable efficient broad-band fiber filter," *IEEE Photon. Technol. Lett.* **11**, 445–447 (1999).
5. K. O. Hill, B. Malo, K. A. Vineberg, F. Bilodeau, D. C. Johnson, and I. Skinner, "Efficient mode conversion in telecommunication fibre using externally written gratings," *Electron. Lett.* **26**, 1270–1272 (1990).
6. P. F. Wysocki, I. B. Judkins, R. P. Espindola, M. Andrejco, and A. M. Vengsarkar, "Broad-band erbium-doped fiber amplifier flattened beyond 40 nm using long-period grating filter," *IEEE Photon. Technol. Lett.* **9**, 1343–1345 (1997).
7. M. Das and K. Thyagarajan, "Dispersion control with use of long-period fiber gratings," *Opt. Lett.* **190**, 159–163 (2001).
8. M. N. Ng, Z. Chen, and K. S. Chiang, "Temperature compensation of long-period fiber grating for refractive-index sensing with bending effect," *IEEE Photon. Technol. Lett.* **14**, 361–362 (2002).
9. J. N. Kutz, B. J. Eggleton, J. B. Stark, and R. E. Slusher, "Nonlinear pulse propagation in long-period fiber gratings: theory and experiment," *IEEE J. Sel. Top. Quantum Electron.* **3**, 1232–1245 (1997).
10. B. J. Eggleton, R. E. Slusher, J. B. Judkins, J. B. Stark, and A. M. Vengsarkar, "All-optical switching in long-period fiber gratings," *Opt. Lett.* **22**, 883–885 (1997).
11. R. E. Slusher, G. Lenz, J. Hodelin, J. Sanghera, L. B. Shaw, and I. D. Aggarwal, "Large Raman gain and nonlinear phase shifts in high-purity  $\text{As}_2\text{S}_3$  chalcogenide fibers," *J. Opt. Soc. Am. B* **21**, 1146–1155 (2004).
12. L. E. Busse, J. A. Moon, J. S. Sanhera, and I. D. Aggarwal, "Chalcogenide fibers deliver high IR power," *Laser Focus World* **32**, 143–145 (1996).
13. P. A. Thielen, L. B. Shaw, P. C. Pureza, V. Q. Nguyen, J. S. Sanghera, and I. D. Aggarwal, "Small-core As–Se fiber for Raman amplification," *Opt. Lett.* **28**, 1406–1408 (2003).
14. V. G. Ta'eed, M. Shokooh-Saremi, L. Fu, D. J. Moss, M. Rochette, I. C. M. Littler, B. J. Eggleton, Y. Ruan, and B. Luther-Davies, "Integrated all-optical pulse regenerator in chalcogenide waveguides," *Opt. Lett.* **30**, 2900–2902 (2005).
15. M. Asobe, T. Kanamori, and K. Kubodera, "Ultrafast all-optical switching using highly nonlinear chalcogenide glass fiber," *IEEE Photon. Technol. Lett.* **29**, 362–365 (1992).
16. M. Asobe, T. Ohara, I. Yokohama, and T. Kaino, "Fabrication of Bragg grating in chalcogenide glass fiber using the transverse holographic method," *Electron. Lett.* **32**, 1611–1613 (1996).
17. M. Shokooh-Saremi, V. G. Ta'eed, N. J. Baker, I. C. M. Littler, D. J. Moss, B. J. Eggleton, Y. Ruan, and B. Luther-Davies, "High-performance Bragg gratings in chalcogenide rib waveguides written with a modified Sagnac interferometer," *J. Opt. Soc. Am. B* **23**, 1323–1330 (2007).
18. N. J. Baker, H. W. Lee, I. C. M. Littler, C. M. de Sterke, B. J. Eggleton, D.-Y. Choi, S. Madden, and B. Luther-Davies, "Sampled Bragg gratings in chalcogenide ( $\text{As}_2\text{S}_3$ ) rib-waveguides," *Opt. Express* **14**, 9451–9459 (2006).
19. D. Pudo, E. C. Mägi, and B. J. Eggleton, "Long-period gratings in chalcogenide fibers," *Opt. Express* **14**, 3763–3766 (2006).
20. I. C. M. Littler, L. B. Fu, E. C. Mägi, D. Pudo, and B. J.

- Eggleton, "Widely tunable, acousto-optic resonances in chalcogenide  $\text{As}_2\text{Se}_3$  fiber," *Opt. Express* **14**, 8088–8095 (2006).
21. V. Rastogi and K. S. Chiang, "Long-period gratings in planar optical waveguides," *Appl. Opt.* **41**, 6351–6355 (2002).
  22. K. S. Chiang, K. P. Lor, C. K. Chow, H. P. Chan, V. Rastogi, and Y. M. Chu, "Widely tunable long-period gratings fabricated in polymer-clad ion-exchanged glass waveguides," *IEEE Photon. Technol. Lett.* **15**, 1094–1096 (2003).
  23. A. Perentos, G. Kostovski, and A. Mitchell, "Polymer long-period raised rib waveguide gratings using nano-imprint lithography," *IEEE Photon. Technol. Lett.* **17**, 2595–2597 (2005).
  24. Q. Liu, K. S. Chiang, and V. Rastogi, "Analysis of corrugated long-period gratings in slab waveguides and their polarization dependence," *J. Lightwave Technol.* **21**, 3399–3405 (2003).
  25. M. Kulishov, "Interdigitated electrode-induced phase grating with an electrically switchable and tunable period," *Appl. Opt.* **38**, 7356–7363 (1999).
  26. K. Finsterbusch, N. J. Baker, V. G. Ta'eed, B. J. Eggleton, D. Choi, S. Madden, and B. Luther-Davis, "Long-period gratings in chalcogenide ( $\text{As}_2\text{S}_3$ ) rib waveguides," *Electron. Lett.* **42**, 1094–1095 (2006).
  27. B. J. Eggleton, P. S. Westbrook, C. A. White, C. Kerbage, R. S. Windeler, and G. L. Burdge, "Cladding-mode-resonances in air-silica microstructure optical fibers," *J. Lightwave Technol.* **18**, 1084–1100 (2000).
  28. M. D. Feit and J. A. Fleck, "Computation of mode properties in optical fiber wave guides by a propagating beam method," *Appl. Opt.* **19**, 1154–1164 (1980).
  29. T. Erdogan, "Fiber grating spectra," *J. Lightwave Technol.* **15**, 1277–1294 (1997).
  30. A. Yariv and P. Yeh, *Optical Waves in Crystals* (Wiley, 1984).
  31. B. Luther-Davis, V. Z. Kolev, M. J. Lederer, N. R. Madsen, J. Giesekus, K.-M. Du, and M. Duering, "Table-top 50 W laser system for ultra-fast laser ablation," *Appl. Phys. A* **79**, 1051–1055 (2004).
  32. Y. Ruan, W. Li, R. Jarvis, N. Madsen, A. Rode, and B. Luther-Davis, "Fabrication and characterization of low loss rib chalcogenide waveguides made by dry etching," *Opt. Express* **12**, 5140–5145 (2004).
  33. R. A. Soref, J. Schmidtchen, and K. Petermann, "Large single-mode rib waveguides in GeSi-Si and Si-on-SiO<sub>2</sub>," *IEEE J. Quantum Electron.* **27**, 1971–1974 (1991).
  34. V. M. Kryshenik, and V. I. Mikla, "Anisotropic phenomena in as-evaporated amorphous chalcogenide thin films," *Mater. Sci. Eng., B* **100**, 292–296 (2003).